



# ATLAS CONF Note

ATLAS-CONF-2017-019



## Search for direct top squark pair production in events with a Higgs or Z boson, and missing transverse momentum in $pp$ collisions at $\sqrt{s} = 13$ TeV with the ATLAS detector

The ATLAS Collaboration

22nd March 2017

A search for direct top squark pair production resulting in events with either a same-flavour opposite-sign dilepton pair with invariant mass compatible with a  $Z$  boson or a pair of jets compatible with a Standard Model (SM) Higgs boson ( $h$ ) is presented. Requirements on additional leptons, jets, jets identified as originating from  $b$ -quarks, and missing transverse momentum are imposed to target the decay products of the top squark pair. The analysis is performed using proton-proton collision data at  $\sqrt{s} = 13$  TeV collected with the ATLAS detector at the LHC in 2015-2016, corresponding to an integrated luminosity of  $36.1 \text{ fb}^{-1}$ . No excess is observed in the data with respect to the expected SM predictions. The results are interpreted in two sets of models. In the first set, direct production of pairs of lighter top squarks ( $\tilde{t}_1$ ) with long decay chains involving  $Z$  or Higgs bosons is considered. The second set includes direct pair production of the heavier top squark pairs ( $\tilde{t}_2$ ) decaying via  $\tilde{t}_2 \rightarrow Z\tilde{t}_1$  or  $\tilde{t}_2 \rightarrow h\tilde{t}_1$ . The results exclude at 95% confidence level  $\tilde{t}_2$  and  $\tilde{t}_1$  masses up to about 870 GeV, extending the exclusion region of supersymmetric parameter space covered by previous LHC searches.

# 1 Introduction

Supersymmetry (SUSY) [1–6] is one of the most studied extensions of the Standard Model (SM). It predicts new bosonic partners for the existing fermions and fermionic partners for the known bosons. If  $R$ -parity is conserved [7], SUSY particles are produced in pairs and the lightest supersymmetric particle (LSP) is stable, providing a possible dark matter candidate. The SUSY partners of the charged (neutral) Higgs bosons and electroweak gauge bosons mix to form the mass eigenstates known as charginos,  $\tilde{\chi}_k^\pm$ ,  $k = 1, 2$  (neutralinos,  $\tilde{\chi}_m^0$ ,  $m = 1, \dots, 4$ ) where the increasing index denotes increasing mass. The scalar partners of right-handed and left-handed quarks,  $\tilde{q}_R$  and  $\tilde{q}_L$ , mix to form two mass eigenstates,  $\tilde{q}_1$  and  $\tilde{q}_2$ , with  $\tilde{q}_1$  defined to be the lighter of the two. To address the SM hierarchy problem [8–11], TeV-scale masses are required [12, 13] for the supersymmetric partners of the gluons (gluinos,  $\tilde{g}$ ) and the top-squarks [14, 15]. Furthermore, the higgsino is required not to be heavier than a few hundred GeV.

Top squark production with Higgs ( $h$ ) or  $Z$  bosons in the decay chain can appear either in production of the lightest top squark mass eigenstate ( $\tilde{t}_1$ ) decaying via  $\tilde{t}_1 \rightarrow t \tilde{\chi}_2^0$  with  $\tilde{\chi}_2^0 \rightarrow h/Z \tilde{\chi}_1^0$ , or in production of the heaviest top squark mass eigenstate ( $\tilde{t}_2$ ) decaying via  $\tilde{t}_2 \rightarrow h/Z \tilde{t}_1$ , as illustrated in Figure 1. Such signals can be discriminated from the SM top-quark pair production ( $t\bar{t}$ ) background by requiring a pair of  $b$ -tagged jets originating from the  $h \rightarrow b\bar{b}$  decay or a same-flavour opposite-sign lepton pair originating from the  $Z \rightarrow \ell^+\ell^-$  decay. Although the pair production of  $\tilde{t}_1$  has a cross-section larger than that of the  $\tilde{t}_2$ , and their decay properties can be similar, searches for the latter can provide additional sensitivity in regions where the  $\tilde{t}_1$  falls in a phase space difficult to access experimentally due to the similarities in kinematics with  $t\bar{t}$  pair production, such as scenarios where the lightest stop is only slightly heavier than the sum of the masses of the top quark and the  $\tilde{\chi}_1^0$ .

Simplified models [16–18] are used for the analysis optimisation and interpretation of the results. In these models, direct top squark pair production is considered and all SUSY particles are decoupled except for the top squarks and the neutralinos involved in their decay. In all cases the  $\tilde{\chi}_1^0$  is assumed to be the LSP. Simplified models featuring direct  $\tilde{t}_1$  production with  $\tilde{t}_1 \rightarrow t \tilde{\chi}_2^0$  and either  $\tilde{\chi}_2^0 \rightarrow Z \tilde{\chi}_1^0$  or  $\tilde{\chi}_2^0 \rightarrow h \tilde{\chi}_1^0$  are considered. Additional simplified models featuring direct  $\tilde{t}_2$  production with  $\tilde{t}_2 \rightarrow Z \tilde{t}_1$  or  $\tilde{t}_2 \rightarrow h \tilde{t}_1$  decays and  $\tilde{t}_1 \rightarrow t \tilde{\chi}_1^0$  are also considered, where the mass difference between the lighter stop and the neutralino is set to 180 GeV, a region of the mass parameter space not excluded by previous searches for  $\tilde{t}_1$  with mass greater than 191 GeV [19].

This notes presents the results of a search for top squarks in final states with  $h$  or  $Z$  bosons at  $\sqrt{s} = 13$  TeV using the data collected by the ATLAS experiment [20] in proton–proton ( $pp$ ) collisions during 2015 and 2016, corresponding to  $36.1 \text{ fb}^{-1}$ . Searches for direct  $\tilde{t}_1$  pair production have been performed by the ATLAS [19, 21, 22] and CMS [23–28] collaborations, while searches for direct  $\tilde{t}_2$  production were performed in the LHC Run 1 at  $\sqrt{s} = 8$  TeV [19, 29, 30].

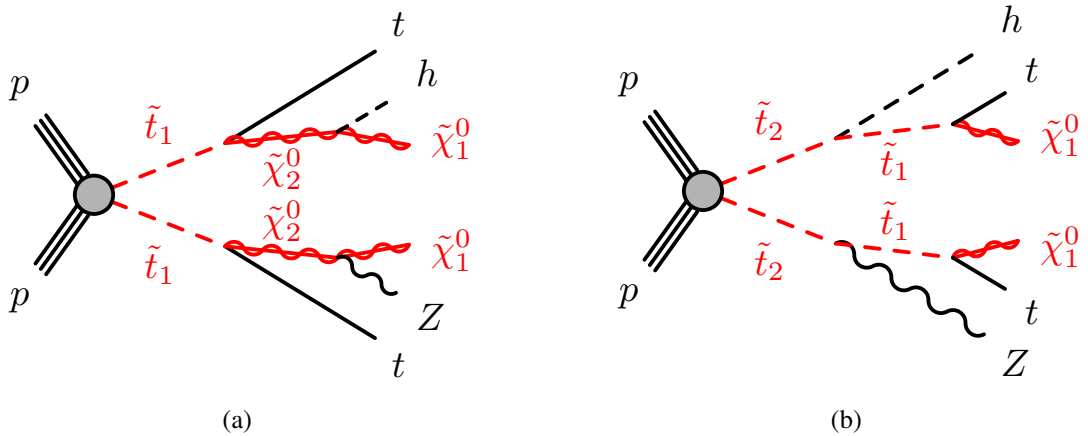


Figure 1: Diagram of the top squark pair production processes considered in this analysis: (a)  $\tilde{t}_1 \rightarrow t \tilde{\chi}_2^0$  and  $\tilde{\chi}_2^0 \rightarrow h/Z \tilde{\chi}_1^0$  decays, and (b)  $\tilde{t}_2 \rightarrow h/Z \tilde{t}_1$  and  $\tilde{t}_1 \rightarrow t \tilde{\chi}_1^0$  decays.

## 2 ATLAS detector

The ATLAS experiment [20] is a multi-purpose particle detector with a forward-backward symmetric cylindrical geometry and nearly  $4\pi$  coverage in solid angle.<sup>1</sup> The interaction point is surrounded by an inner detector (ID), a calorimeter system, and a muon spectrometer.

The ID provides precision tracking of charged particles for pseudorapidities  $|\eta| < 2.5$  and is surrounded by a superconducting solenoid providing a 2 T axial magnetic field. It consists of pixel and silicon-microstrip detectors inside a transition radiation tracker. One significant upgrade for the running period at  $\sqrt{s} = 13$  TeV is the presence of the Insertable B-Layer [31], an additional pixel layer close to the interaction point, which provides high-resolution hits at small radius to improve the tracking performance.

In the pseudorapidity region  $|\eta| < 3.2$ , high-granularity lead/liquid-argon (LAr) electromagnetic (EM) sampling calorimeters are used. A steel/scintillator tile calorimeter measures hadron energies for  $|\eta| < 1.7$ . The endcap and forward regions, spanning  $1.5 < |\eta| < 4.9$ , are instrumented with LAr calorimeters for both the EM and hadronic energy measurements.

The muon spectrometer consists of three large superconducting toroids with eight coils each, a system of trigger and precision-tracking chambers, which provide triggering and tracking capabilities in the ranges  $|\eta| < 2.4$  and  $|\eta| < 2.7$ , respectively.

A two-level trigger system is used to select events [32]. The first-level trigger is implemented in hardware and uses a subset of the detector information. This is followed by the software-based High-Level Trigger stage, which runs offline reconstruction and calibration software, reducing the event rate to about 1 kHz.

<sup>1</sup> ATLAS uses a right-handed coordinate system with its origin at the nominal interaction point (IP) in the centre of the detector and the  $z$ -axis along the beam pipe. The  $x$ -axis points from the IP to the centre of the LHC ring, and the  $y$ -axis points upward. Cylindrical coordinates  $(r, \phi)$  are used in the transverse plane,  $\phi$  being the azimuthal angle around the beam pipe. The pseudorapidity is defined in terms of the polar angle  $\theta$  as  $\eta = -\ln \tan(\theta/2)$ . Rapidity is defined as  $y = 0.5 \ln [(E + p_z)/(E - p_z)]$  where  $E$  denotes the energy and  $p_z$  is the component of the momentum along the beam direction.

Table 1: Simulated signal and background event samples: the corresponding generator, parton shower, cross-section normalisation, PDF set and underlying-event tune are shown.

Physics process	Generator	Parton shower	Cross-section normalisation	PDF set	Tune
SUSY Signals	<code>MADGRAPH5_AMC</code> @NLO 2.2.3 [39]	<code>PYTHIA</code> 8.186 [40]	NLO+NLL [41–45]	NNPDF2.3LO [46]	A14 [47]
$W(\rightarrow \ell\nu) + \text{jets}$	SHERPA 2.2.1 [48]	SHERPA 2.2.1	NNLO [49]	NLO CT10 [46]	SHERPA default
$Z/\gamma^*(\rightarrow \ell\ell) + \text{jets}$	SHERPA 2.2.1	SHERPA 2.2.1	NNLO [49]	NLO CT10	SHERPA default
$t\bar{t}$	POWHEG-BOX v2 [50]	<code>PYTHIA</code> 6.428 [51]	NNLO+NNLL [52–57]	NLO CT10	PERUGIA2012 [58]
Single-top ( $t$ -channel)	POWHEG-BOX v1	<code>PYTHIA</code> 6.428	NNLO+NNLL [59]	NLO CT10f4	PERUGIA2012
Single-top ( $s$ - and $Wt$ -channel)	POWHEG-BOX v2	<code>PYTHIA</code> 6.428	NNLO+NNLL [60, 61]	NLO CT10	PERUGIA2012
$t\bar{t}W/Z/\gamma^*$	<code>MADGRAPH5_AMC</code> @NLO 2.2.2	<code>PYTHIA</code> 8.186	NLO [39]	NNPDF2.3LO	A14
Diboson	SHERPA 2.2.1	SHERPA 2.2.1	Generator NLO	CT10	SHERPA default
$t\bar{t}h$	<code>MADGRAPH5_AMC</code> @NLO 2.2.2	<code>HERWIG</code> 2.7.1 [62]	NLO [63]	CTEQ6L1	A14
$Wh, Zh$	<code>MADGRAPH5_AMC</code> @NLO 2.2.2	<code>PYTHIA</code> 8.186	NLO [63]	NNPDF2.3LO	A14
$t\bar{t}WW, t\bar{t}t\bar{t}$	<code>MADGRAPH5_AMC</code> @NLO 2.2.2	<code>PYTHIA</code> 8.186	NLO [39]	NNPDF2.3LO	A14
$tZ, tWZ, t\bar{t}t$	<code>MADGRAPH5_AMC</code> @NLO 2.2.2	<code>PYTHIA</code> 8.186	LO	NNPDF2.3LO	A14
Triboson	SHERPA 2.2.1	SHERPA 2.2.1	Generator LO, NLO	CT10	SHERPA default

### 3 Dataset and simulated event samples

The data were collected by the ATLAS detector during 2015 with a peak instantaneous luminosity of  $\mathcal{L} = 5.2 \times 10^{33} \text{ cm}^{-2}\text{s}^{-1}$ , and during 2016 with a peak instantaneous luminosity of  $\mathcal{L} = 1.4 \times 10^{34} \text{ cm}^{-2}\text{s}^{-1}$ , resulting in a mean number of additional  $pp$  interactions per bunch crossing (pile-up) of  $\langle \mu \rangle = 14$  in 2015 and  $\langle \mu \rangle = 24$  in 2016. Data quality requirements are applied to ensure that all sub-detectors were operating at nominal conditions, and that LHC beams were in stable-collision mode. The integrated luminosity of the resulting dataset is  $36.1 \text{ fb}^{-1}$  with a preliminary uncertainty of  $\pm 3.2\%$ . The luminosity and its uncertainty are derived following a methodology similar to that detailed in Ref. [33] from a preliminary calibration of the luminosity scale using a pair of  $x$ – $y$  beam-separation scans performed in August 2015 and May 2016.

Monte Carlo (MC) simulated event samples are used to aid in the estimation of the background from SM processes and to model the SUSY signal. The generator, parton shower and hadronisation, cross-section normalisation, parton distribution function (PDF) set and underlying-event tune of these samples are given in Table 1, and more details on the generator configurations can be found in Refs. [34–37]. Cross-sections calculated at next-to-next-to leading order (NNLO) in QCD including resummation of next-to-next-to-leading logarithmic (NNLL) soft-gluon terms are used for top-quark production processes. For production of top-quark pairs in association with vector and Higgs bosons, cross-sections calculated at next-to-leading order (NLO) are used, and the generator cross-sections by SHERPA (at NLO for most of the processes) are used when normalising the multi-boson backgrounds. In all MC samples, except those produced by SHERPA, the EvtGEN v1.2.0 program [38] is used to model the properties of the bottom and charm hadron decays.

SUSY signal samples are generated from leading-order (LO) matrix elements with up to two extra partons, using the `MADGRAPH5_AMC`@NLO v2.2.3 generator interfaced to `PYTHIA` 8.186 with the A14 tune for the modelling of the SUSY decay chain, parton showering, hadronisation and the description of the underlying event. Parton luminosities are provided by the NNPDF23LO PDF set. Jet–parton matching is realised following the CKKW-L prescription [64], with a matching scale set to one quarter of the pair-produced superpartner mass. In all cases, the mass of the top quark is fixed at 172.5 GeV. Signal cross-sections are calculated to NLO in the strong coupling constant, adding the resummation of soft-gluon

emission at next-to-leading-logarithmic accuracy (NLO+NLL) [45, 65, 66]. The nominal cross-section and the uncertainty are taken from an envelope of cross-section predictions using different PDF sets and factorisation and renormalisation scales, as described in Ref. [67].

To simulate the effects of additional  $pp$  collisions in the same and nearby bunch crossings, additional interactions are generated using the soft QCD processes of PYTHIA 8.186 with the A2 tune [68] and the MSTW2008LO PDF set [69], and overlaid onto each simulated hard-scatter event. The MC samples are reweighted so that the pile-up distribution matches the one observed in the data. The MC samples are processed through an ATLAS detector simulation [70] based on GEANT4 [71] or, in the case of  $t\bar{t}$  and the SUSY signal samples, a fast simulation using a parameterisation of the calorimeter response and GEANT4 for the other parts of the detector [72]. All MC samples are reconstructed in the same manner as the data.

## 4 Event selection

Candidate events are required to have a reconstructed vertex [73] with at least two associated tracks with transverse momentum ( $p_T$ ) larger than 400 MeV that are consistent with originating from the beam collision region in the  $x$ – $y$  plane. The vertex with the highest scalar sum of the squared transverse momentum of the associated tracks is considered to be the primary vertex of the event.

Electron candidates are reconstructed from isolated electromagnetic calorimeter energy deposits matched to ID tracks and are required to have  $|\eta| < 2.47$ , a transverse momentum  $p_T > 10$  GeV, and to pass a “loose” likelihood-based identification requirement [74, 75]. The likelihood input variables include measurements of calorimeter shower shapes and of track properties from the ID.

Muon candidates are reconstructed in the region  $|\eta| < 2.5$  from muon spectrometer tracks matching ID tracks. Candidate muons must have  $p_T > 10$  GeV and pass the medium identification requirements defined in Ref. [76], based on the number of hits in the different ID and muon spectrometer subsystems, and on the significance of the charge to momentum ratio  $q/p$ .

Jets are reconstructed from three-dimensional energy clusters in the calorimeter [77] using the anti- $k_T$  jet clustering algorithm [78] with a radius parameter  $R = 0.4$ . Only jet candidates with  $p_T > 30$  GeV and  $|\eta| < 2.5$  are considered as selected jets in the analysis. Jets are calibrated as described in Refs. [79, 80], and the expected average energy contribution from pile-up clusters is subtracted according to the jet area [79]. In order to reduce the effects of pile-up, for jets with  $p_T < 60$  GeV and  $|\eta| < 2.4$  a significant fraction of the tracks associated with each jet must have an origin compatible with the primary vertex, as defined by the jet vertex tagger [81].

Events are discarded if they contain any jet with  $p_T > 20$  GeV failing basic quality selection criteria that reject detector noise and non-collision backgrounds [82].

Identification of jets containing  $b$ -hadrons ( $b$ -tagging) is performed with a multivariate discriminant that makes use of track impact parameters and reconstructed secondary vertices [83, 84]. A requirement is chosen corresponding to a 77% average efficiency obtained for  $b$ -quark jets in simulated  $t\bar{t}$  events. The rejection factors for light-quark jets,  $c$ -quark jets and hadronically-decaying  $\tau$  leptons in simulated  $t\bar{t}$  events are approximately 380, 12 and 54, respectively. To compensate for differences between data and MC simulation in the  $b$ -tagging efficiencies and mis-tag rates, correction factors are applied to the simulated samples [84].

Jet candidates within  $\Delta R = \sqrt{(\Delta y)^2 + (\Delta\phi)^2} < 0.2$  of a lepton candidate are discarded, unless the jet has a value of the  $b$ -tagging discriminant larger than the value corresponding to approximately 85%  $b$ -tagging efficiency, in which case the lepton is discarded since it is likely originating from a semileptonic  $b$ -hadron decay. Any remaining electron candidate within  $\Delta R < 0.4$  of a non-pile-up jet, and any muon candidate within  $\Delta R < \min\{0.4, 0.04 + p_T(\ell)/10 \text{ GeV}\}$  of a non-pile-up jet is discarded. In the latter case, if the jet has fewer than three associated tracks or the muon  $p_T$  is larger than half of the jet  $p_T$ , the muon is retained and the jet is discarded instead to avoid inefficiencies for high-energy muons undergoing significant energy loss in the calorimeter. Any muon candidate reconstructed with ID and calorimeter information only that shares an ID track with an electron candidate is removed. Finally, any electron candidate sharing an ID track with the remaining muon candidates is also removed.

Tighter requirements on the lepton candidates are imposed, which are then referred to as “signal” electrons or muons. Signal electrons must satisfy the “medium” likelihood-based identification requirement as defined in Ref. [74, 75]. Signal electrons (muons) must have  $p_T > 20 \text{ GeV}$ . The associated tracks must have a significance of the transverse impact parameter with respect to the reconstructed primary vertex,  $d_0$ , of  $|d_0|/\sigma(d_0) < 5(3)$  and a longitudinal impact parameter with respect to the reconstructed primary vertex,  $z_0$ , satisfying  $|z_0 \sin \theta| < 0.5 \text{ mm}$ . Isolation requirements are applied to both the signal electrons and muons. The scalar sum of the  $p_T$  of tracks within a variable-size cone around the lepton, excluding its own track, must be less than 6% of the lepton  $p_T$ . The radius of the track isolation cone for electrons (muons) is given by the smaller of  $\Delta R = 10 \text{ GeV}/p_T$  and  $\Delta R = 0.2$  (0.3), that is, a cone of size 0.2 (0.3) at low  $p_T$  but narrower for high- $p_T$  leptons. In addition, in the case of electrons the energy of calorimeter energy clusters in a cone of  $\Delta R_\eta = 0.2$  around the electron (excluding the deposition from the electron itself) must be less than 6% of the electron  $p_T$ .

Simulated events are corrected to account for minor differences in the signal lepton trigger, reconstruction, identification and isolation efficiencies between data and MC simulation.

The missing transverse momentum vector, whose magnitude is denoted by  $E_T^{\text{miss}}$ , is defined as the negative vector sum of the transverse momenta of all identified physics objects (electrons, photons, muons, jets) and an additional soft term. The soft term is constructed from all tracks originating from the primary vertex and that are not associated with any physics object. In this way, the  $E_T^{\text{miss}}$  is adjusted for the best calibration of the jets and the other identified physics objects above, while maintaining pile-up independence in the soft term [85, 86].

The events are classified in a further step into two exclusive categories: at least three leptons plus a  $b$ -tagged jet ( $3\ell 1b$  selection, aiming at top squark decays involving  $Z$  bosons), or at least four  $b$ -tagged jets and one or two leptons ( $1\ell 4b$  selection, aiming at top squark decays involving Higgs bosons).

In the  $3\ell 1b$  selection, events are accepted if they pass a trigger requiring either two electrons, two muons or an electron and a muon. In the  $1\ell 4b$  selection, events are accepted if they pass a trigger requiring an isolated electron or muon. The trigger-level requirements on the  $p_T$ , identification and isolation criteria of the leptons involved in the trigger decision are looser than those applied offline to ensure that trigger efficiencies are constant in the relevant phase space [32].

Additional requirements beyond the preselection classification are applied depending on the final state, as described in the following. These requirements are optimized to maximize the discovery significance using the simplified models featuring  $\tilde{t}_2$  production with  $\tilde{t}_2 \rightarrow Z\tilde{t}_1$  or  $\tilde{t}_2 \rightarrow h\tilde{t}_1$  decays.

## 4.1 3 $\ell$ 1 $b$ selection

Events of interest are selected if they contain at least three signal leptons (electrons or muons), with at least one same-flavour opposite-sign lepton pair whose invariant mass is compatible with the  $Z$  boson mass ( $|m_{\ell\ell} - m_Z| < 15$  GeV, with  $m_Z = 91.2$  GeV). To maximise the sensitivity in different regions of the mass parameter space, three overlapping signal regions (SRs) are defined as shown in Table 2. Signal region  $SR_A^{3\ell 1b}$  is optimized for large mass splitting between the  $\tilde{t}_2$  and  $\tilde{\chi}_1^0$ , where the  $Z$  boson in the  $\tilde{t}_2 \rightarrow Z\tilde{t}_1$  decay is boosted, and large  $p_T^{\ell\ell}$  and leading jet  $p_T$  are required. Signal region  $SR_B^{3\ell 1b}$  covers the intermediate case, featuring slightly softer kinematic requirements than in  $SR_A^{3\ell 1b}$ . Signal region  $SR_C^{3\ell 1b}$  is designed to improve the sensitivity for compressed spectra ( $m_{\tilde{t}_2} \gtrsim m_{\tilde{\chi}_1^0} + m_t + m_Z$ ) with softer jet  $p_T$  requirements and an upper bound on  $p_T^{\ell\ell}$ .

Table 2: Definition of the signal regions used in the 3 $\ell$ 1 $b$  selection (see text for details).

Requirement / Region	$SR_A^{3\ell 1b}$	$SR_B^{3\ell 1b}$	$SR_C^{3\ell 1b}$
Number of leptons	$\geq 3$	$\geq 3$	$\geq 3$
$n_{b\text{-tagged jets}}$	$\geq 1$	$\geq 1$	$\geq 1$
$ m_{\ell\ell} - m_Z $ [GeV]	$< 15$	$< 15$	$< 15$
Leading lepton $p_T$ [GeV]	$> 40$	$> 40$	$> 40$
Leading jet $p_T$ [GeV]	$> 250$	$> 80$	$> 60$
Leading $b$ -tagged jet $p_T$ [GeV]	$> 40$	$> 40$	$> 30$
$n_{\text{jets}} (p_T > 30 \text{ GeV})$	$\geq 6$	$\geq 6$	$\geq 5$
$E_T^{\text{miss}}$ [GeV]	$> 100$	$> 180$	$> 140$
$p_T^{\ell\ell}$ [GeV]	$> 150$	–	$< 80$

## 4.2 1 $\ell$ 4 $b$ selection

Similarly to the 3 $\ell$ 1 $b$  case, three overlapping SRs are defined in the 1 $\ell$ 4 $b$  selection to have a good sensitivity in different regions of the mass parameter space. Only events with one or two signal leptons are selected to ensure orthogonality with the SRs in the 3 $\ell$ 1 $b$  selection, with at least one lepton with  $p_T > 30$  GeV, and the electron candidates are also required to satisfy the *tight* likelihood-based identification requirement as defined in Refs. [74, 75]. These SRs are defined as shown in Table 3.

Signal region  $SR_A^{1\ell 4b}$  is optimized for large mass splitting between the  $\tilde{t}_2$  and  $\tilde{\chi}_1^0$ , where the Higgs boson in the  $\tilde{t}_2 \rightarrow h\tilde{t}_1$  decay is boosted. In this signal region, the pair of  $b$ -tagged jets with the smallest  $\Delta R^{bb}$  is required to have an invariant mass consistent with the Higgs boson mass ( $|m_{bb} - m_h| < 15$  GeV, with  $m_h = 125$  GeV), and the transverse momentum of the system formed by these two  $b$ -tagged jets ( $p_T^{bb}$ ) is required to be above 300 GeV. Signal region  $SR_B^{1\ell 4b}$  covers the intermediate case, featuring slightly harder kinematic requirements than  $SR_A^{1\ell 4b}$ . Finally, signal region  $SR_C^{1\ell 4b}$  is designed to be sensitive to compressed spectra ( $m_{\tilde{t}_2} \gtrsim m_{\tilde{\chi}_1^0} + m_t + m_h$ ). This region has softer jet  $p_T$  requirements and an upper bound on the  $p_T$  of the leading  $b$ -tagged jet. Signal region  $SR_A^{1\ell 4b}$  includes requirements on  $H_T$  (computed as the scalar sum of the  $p_T$  of all the jets in the event), while both signal regions  $SR_B^{1\ell 4b}$  and  $SR_C^{1\ell 4b}$

include requirements on the transverse mass  $m_T$  (computed using the  $E_T^{\text{miss}}$  and the lepton momentum:  $m_T = \sqrt{2p_T^\ell E_T^{\text{miss}}(1 - \cos(\Delta\phi(\ell, E_T^{\text{miss}})))}$ ).

Table 3: Definition of the signal regions used in the  $1\ell 4b$  selection (see text for details).

Requirement / Region	SR <sub>A</sub> <sup>1<math>\ell</math>4<math>b</math></sup>	SR <sub>B</sub> <sup>1<math>\ell</math>4<math>b</math></sup>	SR <sub>C</sub> <sup>1<math>\ell</math>4<math>b</math></sup>
Number of leptons	1–2	1–2	1–2
$n_b$ –tagged jets	$\geq 4$	$\geq 4$	$\geq 4$
$m_T$ [GeV]	–	$> 150$	$> 125$
$H_T$ [GeV]	$> 1000$	–	–
$E_T^{\text{miss}}$ [GeV]	$> 120$	$> 150$	$> 150$
Leading $b$ -tagged jet $p_T$ [GeV]	–	–	$< 140$
$m_{bb}$ [GeV]	95–155	–	–
$p_T^{bb}$ [GeV]	$> 300$	–	–
$n_{\text{jets}}$ ( $p_T > 60$ GeV)	$\geq 6$	$\geq 5$	–
$n_{\text{jets}}$ ( $p_T > 30$ GeV)	–	–	$\geq 7$

## 5 Background estimation

The main SM background processes satisfying the SR requirements are estimated by simulation, which is normalized and verified in separate statistically-independent regions of the phase space. Dedicated control regions (CRs) enhanced in a particular background component, such as the production of top-quark pairs in association with a  $Z$  boson ( $t\bar{t}Z$ ) and multi-boson production in the  $3\ell 1b$  selection, and  $t\bar{t}$  in the  $1\ell 4b$  selection, are used for the normalisation. For each signal region, a simultaneous “background” fit is performed to the number of events found in the CRs, using a statistical minimisation based on likelihoods with the HistFitter package [87]. In each fit, the normalisations of the background contributions having dedicated CRs are allowed to float, while the other backgrounds are determined directly using simulation or from additional independent studies in data. Whenever possible, the agreement of the background prediction with data is compared in dedicated validation regions (VRs), which are not used to constrain the background normalization or nuisance parameters in the fit. When setting 95% CL upper limits on the cross-section of specific SUSY models, the simultaneous fits also include the observed yields in the SR.

Systematic uncertainties in the MC simulation affect the ratio of the expected yields in the different regions and are taken into account to determine the uncertainty on the background prediction. Each uncertainty source is described by a single nuisance parameter, and correlations between background processes and selections are taken into account. The fit does not affect either the uncertainty, nor the central value of these nuisance parameters. The systematic uncertainties considered in the fit are described in Section 6.

### 5.1 Background estimation in the $3\ell 1b$ selection

The dominant SM background contribution to the SRs in the  $3\ell 1b$  selection is expected to be from  $t\bar{t}Z$ , with minor contribution from multi-boson production (mainly  $WZ$ ) and backgrounds containing fake

and non-prompt leptons (mainly  $t\bar{t}$ ). The normalisation of the main backgrounds ( $t\bar{t}Z$ , multi-boson) is obtained by fitting the yield to the observed data in two control regions, then extrapolating this yield to the SRs as described above. Other background sources ( $t\bar{t}W$ ,  $t\bar{t}h$  and rare SM processes), which provide a sub-dominant contribution to the SRs, are determined from MC simulation only.

The fake and non-prompt lepton background is estimated from data with a method similar to that described in Refs. [88, 89]. Two types of lepton identification criteria are defined for this evaluation: “tight” and “loose”, corresponding to the signal and candidate electrons and muons described in Section 4. The leading lepton is considered to be prompt, which is a valid assumption in >95% of the cases according to simulations. The method makes use of the number of observed events with the second and third leading lepton being loose-loose, loose-tight, tight-loose and tight-tight in each region. The probability for prompt leptons passing the loose selection criteria to also pass the tight selection is measured on data using a  $Z \rightarrow \ell^+\ell^-$  ( $\ell = e, \mu$ ) enriched sample. The equivalent probability for fake or non-prompt leptons is measured using events with one electron and one muon with the same charge. The number of events with one or two fake or non-prompt leptons is calculated from these probabilities and the number of observed events with loose and tight leptons. The modelling of the fake and non-prompt lepton background is validated in events passing a selection similar to the SRs, but removing the  $E_T^{\text{miss}}$  and inverting the  $m_{\ell\ell}$  requirements.

The two dedicated control regions used for the  $t\bar{t}Z$  ( $\text{CR}_{t\bar{t}Z}^{3\ell 1b}$ ) and multi-boson ( $\text{CR}_{VV}^{3\ell 1b}$ ) background estimation in this selection are defined as shown in Table 4. To ensure orthogonality with the SRs, an upper bound on  $E_T^{\text{miss}} < 100$  GeV is required in  $\text{CR}_{t\bar{t}Z}^{3\ell 1b}$ , while a  $b$ -jet veto is applied in  $\text{CR}_{VV}^{3\ell 1b}$ .

Table 4: Definition of the control regions used in the  $3\ell 1b$  selection.

Requirement / Region	$\text{CR}_{t\bar{t}Z}^{3\ell 1b}$	$\text{CR}_{VV}^{3\ell 1b}$
Number of leptons	$\geq 3$	$\geq 3$
$ m_{\ell\ell} - m_Z $ [GeV]	$< 15$	$< 15$
Leading lepton $p_T$ [GeV]	$> 40$	$> 40$
Leading jet $p_T$ [GeV]	$> 60$	$> 30$
$n_b$ -tagged jets	$\geq 1$	0
$n_{\text{jets}}(p_T > 30 \text{ GeV})$	$\geq 4$	$\geq 4$
$E_T^{\text{miss}}$ [GeV]	$< 100$	–
$p_T^{\ell\ell}$ [GeV]	–	–

Table 5 shows the observed and expected yields in the two CRs for each background source, and Figure 2 shows the  $n_{\text{jets}}$  distribution in these regions. The normalisation factors for the  $t\bar{t}Z$  and multi-boson backgrounds do not exceed 30% and a good agreement is observed between the data and post-fit simulation jet multiplicity distribution.

## 5.2 Background estimation in the $1\ell 4b$ selection

The dominant SM background contribution to the SRs in the  $1\ell 4b$  selection is expected to be top-quark pairs ( $t\bar{t}$ ) production, amounting to more than 80% of the total background. The normalisation of the  $t\bar{t}$

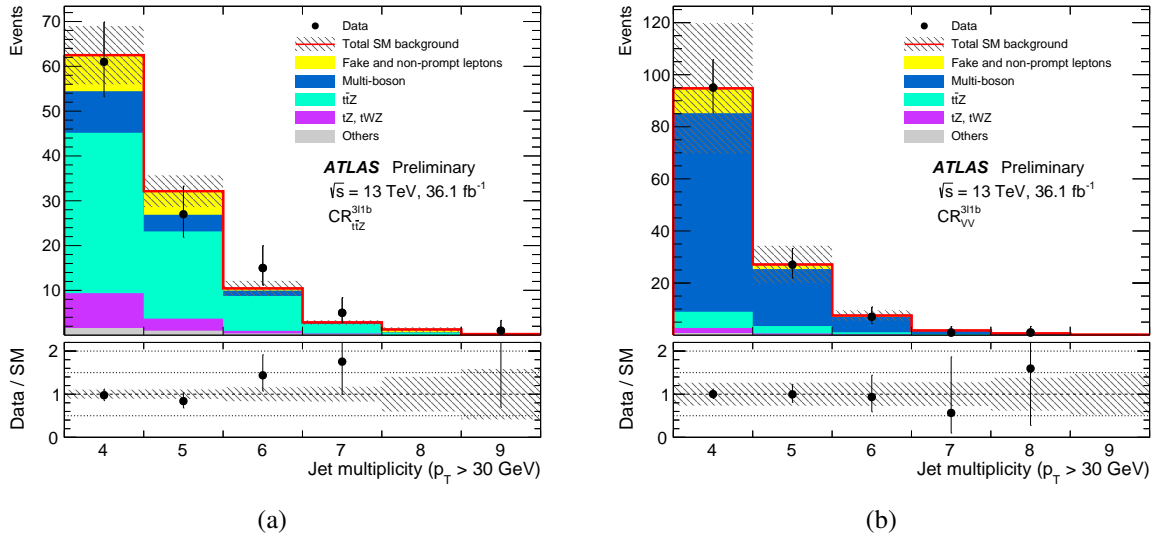


Figure 2: Jet multiplicity distributions in control regions (a)  $\text{CR}_{t\bar{t}Z}^{3\ell1b}$  and (b)  $\text{CR}_{VV}^{3\ell1b}$ , after normalising the  $t\bar{t}Z$  and multi-boson background processes via the simultaneous fit described in Section 5. The contributions from all SM backgrounds are shown as a histogram stack; the bands represent the total uncertainty on the background prediction. The “Others” category contains the contributions from  $t\bar{t}h$ ,  $t\bar{t}WW$ ,  $t\bar{t}t$ ,  $t\bar{t}t\bar{t}$ ,  $Wh$ , and  $Zh$  production. The last bin in both figures contains the overflow. The lower panels show the ratio of the observed data to the total SM background expectation, with bands representing the total uncertainty on the background prediction.

Table 5: Background fit results for the control regions in the  $3\ell1b$  selection. The nominal expectations from MC simulation are given for comparison for those backgrounds ( $t\bar{t}Z$ , multi-boson) that are normalised to data. The “Others” category contains the contributions from  $t\bar{t}h$ ,  $t\bar{t}WW$ ,  $t\bar{t}t$ ,  $t\bar{t}t\bar{t}$ ,  $Wh$ , and  $Zh$  production. Combined statistical and systematic uncertainties are given. The individual uncertainties can be correlated and do not necessarily add in quadrature to the total systematic uncertainty. Events with fake or non-prompt leptons are estimated with the data-driven technique described in Section 5.

	$\text{CR}_{t\bar{t}Z}^{3\ell1b}$	$\text{CR}_{VV}^{3\ell1b}$
Observed events	109	131
Total (post-fit) SM events	$109 \pm 10$	$131 \pm 11$
Fit output, multi-boson	$14.5 \pm 2.7$	$105 \pm 13$
Fit output, $t\bar{t}Z$	$66 \pm 14$	$10.2 \pm 2.7$
Fake and non-prompt leptons	$14 \pm 6$	$12 \pm 7$
$tZ, tWZ$	$11 \pm 6$	$2.7 \pm 1.4$
Others	$3.2 \pm 0.5$	$1.0 \pm 0.3$
Fit input, multi-boson	19	137
Fit input, $t\bar{t}Z$	73	11.2

background for each of the three SRs is obtained by fitting the yield to the observed data in a dedicated CR, then extrapolating this yield to the SRs as described above. Other background sources (single top,  $t\bar{t}h$  and rare SM processes), which provide a sub-dominant contribution to the SRs, are determined from MC

simulation only. The contribution from events with fake and non-prompt leptons is found to be negligible in this selection. The description of the three  $t\bar{t}$  CRs (named  $CR_{t\bar{t},A}^{1\ell4b}$ ,  $CR_{t\bar{t},B}^{1\ell4b}$  and  $CR_{t\bar{t},C}^{1\ell4b}$ ) can be found in Table 6. They are designed to have kinematic properties resembling as closely as possible those of each of the three SRs ( $SR_A^{1\ell4b}$ ,  $SR_B^{1\ell4b}$  and  $SR_C^{1\ell4b}$ , respectively), while having a high purity in  $t\bar{t}$  background and small contamination from signal. The CRs are built by inverting the SR requirements on  $E_T^{\text{miss}}$  and relaxing or inverting those on  $m_{bb}$  or  $m_T$ . Figure 3 shows the jet multiplicity distributions in these CRs. In a similar manner, three validation regions (named  $VR_A^{1\ell4b}$ ,  $VR_B^{1\ell4b}$  and  $VR_C^{1\ell4b}$ ) are defined, each of them corresponding to a different CR, with the same requirements on  $E_T^{\text{miss}}$  as the SR and relaxing or inverting the requirements on  $m_{bb}$ ,  $m_T$  or jet multiplicity, as shown in Table 6. These VRs are used to provide a statistically independent cross-check of the extrapolation in a selection close to that of the SR but with small signal contamination. Table 7 shows the observed and expected yields in the CRs and VRs for each background source. The large correction to  $t\bar{t}$  normalization after the background fit has been observed in other analyses [90] and is due to a mismodelling of the  $t\bar{t} + b\bar{b}, c\bar{c}$  component in the MC simulation. The background prediction is in agreement with the observed data in all VRs.

Table 6: Summary of selection criteria for the control and validation regions in the  $1\ell4b$  selection.

Requirement / Region	$CR_{t\bar{t},A}^{1\ell4b}$	$VR_A^{1\ell4b}$	$CR_{t\bar{t},B}^{1\ell4b}$	$VR_B^{1\ell4b}$	$CR_{t\bar{t},C}^{1\ell4b}$	$VR_C^{1\ell4b}$
Number of leptons	1–2	1–2	1–2	1–2	1–2	1–2
$n_b$ –tagged jets	$\geq 4$	$\geq 4$	$\geq 4$	$\geq 4$	$\geq 4$	$\geq 4$
$m_T$ [GeV]	–	–	$>100$	$>150$	$<125$	$<125$
$E_T^{\text{miss}}$ [GeV]	$<120$	$>120$	$<150$	$>150$	$<150$	$>150$
Leading $b$ -tagged jet $p_T$ [GeV]	–	–	–	–	$<140$	$<140$
$m_{bb}$ [GeV]	95–155	$\notin [95,155]$	–	–	–	–
$n_{\text{jets}}$ ( $p_T > 60$ GeV)	$\geq 5$	$\geq 5$	$\geq 5$	$\leq 4$	–	–
$n_{\text{jets}}$ ( $p_T > 30$ GeV)	–	–	–	–	$\geq 7$	$\geq 7$

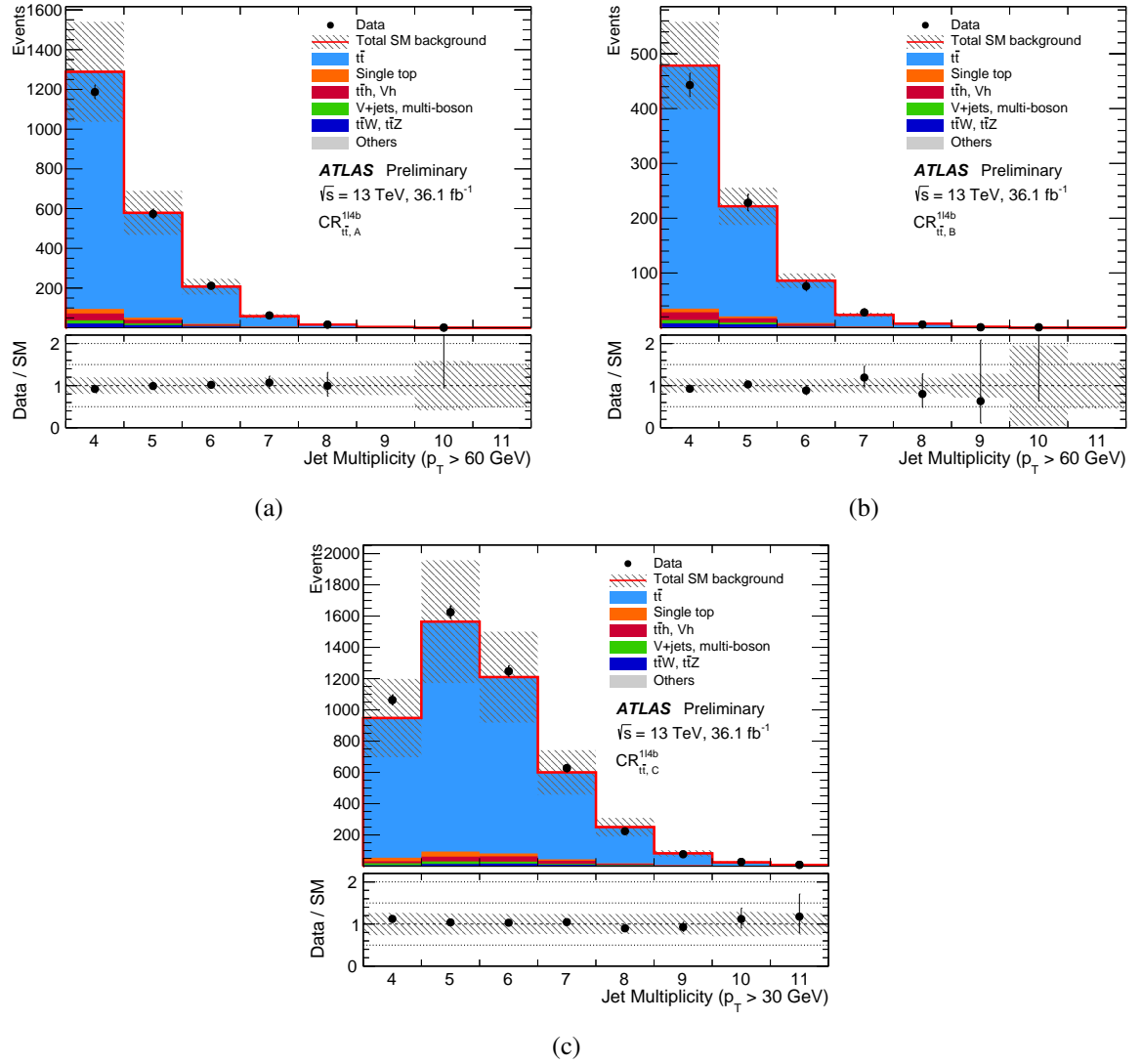


Figure 3: Jet multiplicity distributions in control regions (a)  $CR_{t\bar{t},A}^{1\ell4b}$  (b)  $CR_{t\bar{t},B}^{1\ell4b}$  and (c)  $CR_{t\bar{t},C}^{1\ell4b}$  after normalising the  $t\bar{t}$  background process via the simultaneous fit described in Section 5. The  $t\bar{t}$  background normalisation is constrained to the data observation for jet multiplicity values above the requirements shown on Table 6. The contributions from all SM backgrounds are shown as a histogram stack; the bands represent the total uncertainty. The “Others” category contains the contributions from  $tth$ ,  $t\bar{t}WW$ ,  $t\bar{t}t$ ,  $t\bar{t}\bar{t}$ ,  $Wh$ , and  $Zh$  production. The last bin in all figures contains the overflow. The lower panels show the ratio of the observed data to the total SM background expectation, with the bands representing the total uncertainty on the background prediction.

Table 7: Background fit results for the control and validation regions in the  $1\ell 4b$  selection. The nominal expectations from MC simulation are given for comparison for the  $t\bar{t}$  background, which is normalised to data. The “Others” category contains the contributions from  $t\bar{t}WW$ ,  $t\bar{t}t$ ,  $t\bar{t}t\bar{t}$ ,  $tZ$ , and  $tWZ$  production. Combined statistical and systematic uncertainties are given. The individual uncertainties can be correlated and do not necessarily add in quadrature to the total systematic uncertainty.

	$CR_{t\bar{t},A}^{1\ell 4b}$	$VR_A^{1\ell 4b}$	$CR_{t\bar{t},B}^{1\ell 4b}$	$VR_B^{1\ell 4b}$	$CR_{t\bar{t},C}^{1\ell 4b}$	$VR_C^{1\ell 4b}$
Observed events	863	258	340	86	963	84
Total (post-fit) SM events	$863 \pm 29$	$266 \pm 34$	$340 \pm 18$	$96 \pm 13$	$963 \pm 31$	$90 \pm 11$
Fit output, $t\bar{t}$	$783 \pm 33$	$235 \pm 33$	$307 \pm 19$	$88 \pm 12$	$891 \pm 33$	$82 \pm 10$
Single top	$16 \pm 5$	$9.0 \pm 2.1$	$5.5 \pm 1.8$	$1.7 \pm 0.9$	$12.2 \pm 2.4$	$2.5 \pm 1.3$
$V + \text{jets}$ , multi-boson	$11.8 \pm 2.9$	$3.1 \pm 1.1$	$4.7 \pm 1.4$	$0.15^{+0.20}_{-0.15}$	$9.8 \pm 2.1$	$1.0 \pm 0.4$
$t\bar{t}h$ , $Vh$	$27 \pm 4$	$7.9 \pm 1.3$	$12.7 \pm 2.0$	$3.9 \pm 0.7$	$31 \pm 5$	$2.7 \pm 0.6$
$t\bar{t}W$ , $t\bar{t}Z$	$19 \pm 4$	$7.2 \pm 1.6$	$7.1 \pm 1.7$	$2.2 \pm 0.5$	$15.6 \pm 3.1$	$1.5 \pm 0.5$
Others	$5.0 \pm 2.6$	$3.6 \pm 1.9$	$3.2 \pm 1.7$	$0.57 \pm 0.31$	$2.7 \pm 1.4$	$0.62 \pm 0.32$
Fit input, $t\bar{t}$	495	148	175	50	578	53

## 6 Systematic Uncertainties

The primary sources of systematic uncertainties are related to the jet energy scale, the jet energy resolution, the theoretical and the MC modelling uncertainties on the background determined using CRs ( $t\bar{t}Z$  and multi-bosons on the  $3\ell 1b$  selection, as well as  $t\bar{t}$  on the  $1\ell 4b$  selection). The statistical uncertainty of the simulated event samples is taken into account as well. The effects of the systematic uncertainties is evaluated for all signal samples and background processes. Since the normalisation of the dominant background processes is extracted in dedicated CRs, the systematic uncertainties only affect the extrapolation to the SRs in these cases.

The jet energy scale and resolution uncertainties are derived as a function of the  $p_T$  and  $\eta$  of the jet, as well as of the pile-up conditions and the jet flavour composition of the selected jet sample. They are determined using a combination of simulated and data samples, through measurements of the jet response asymmetry in dijet,  $Z$ +jet and  $\gamma$ +jet events [91]. Uncertainties associated to the modelling of the  $b$ -tagging efficiencies for  $b$ -jets,  $c$ -jets and light-flavour jets [92, 93] are also considered.

The systematic uncertainties related to the modelling of  $E_T^{\text{miss}}$  in the simulation are estimated by propagating the uncertainties on the energy and momentum scale of each of the physics objects, as well as the uncertainties on the soft-term scale and resolution [85].

Other detector-related systematic uncertainties, such as those on lepton reconstruction efficiency, energy scale, energy resolution and on the modelling of the trigger [75, 94], are found to have a small impact on the results.

The uncertainties on the modelling of the  $t\bar{t}$  and single-top backgrounds in simulation in the  $1\ell 4b$  selection are estimated by varying the renormalisation and factorisation scales, as well as the amount of initial- and final-state radiation used to generate the samples [34]. Additional uncertainties on the parton-shower modelling are assessed as the difference between the predictions from POWHEG showered with PYTHIA and HERWIG, and on the generator choice by comparing POWHEG and MADGRAPH5\_AMC@NLO [34], in both cases showered with PYTHIA.

The diboson background MC modelling uncertainties are estimated by varying the renormalisation, factorisation and resummation scales used to generate the samples [95]. For  $t\bar{t}Z$ , the predictions from the MADGRAPH5\_AMC@NLO and SHERPA generators are compared, and the uncertainties related to the choice of the renormalisation and factorisation scales are assessed by varying the corresponding generator parameters up and down by a factor of two around their nominal values [96].

The cross-sections used to normalise the MC samples are varied according to the uncertainty on the cross-section calculation, that is, 6% for diboson, 13% for  $t\bar{t}W$  and 12%  $t\bar{t}Z$  production [39]. For  $t\bar{t}WW$ ,  $tZ$ ,  $tWZ$ ,  $t\bar{t}h$ ,  $t\bar{t}\bar{t}$ ,  $t\bar{t}t\bar{t}$ , and tribosons production processes, which constitute a small background, a 50% uncertainty on the event yields is assumed.

Systematic uncertainties are assigned to the fake and non-prompt lepton background estimate in the  $3\ell 1b$  selection to account for potentially different compositions (heavy flavour, light flavour or conversions) between the signal and control regions, as well as the contamination from prompt leptons in the regions used to measure the probabilities for loose fake and non-prompt leptons to pass the tight signal criteria.

Table 8 summarises the contributions of the different sources of systematic uncertainty in the total SM background predictions in the signal regions. The dominant systematic uncertainties on the  $3\ell 1b$  SRs are

Table 8: Summary of the main systematic uncertainties and their impact (in %) on the total SM background prediction in each of the signal regions studied. The total systematic uncertainty can be different from the sum in quadrature of individual sources due to the correlations between them resulting from the fit to the data. The quoted theoretical uncertainties include modelling and cross-section uncertainties.

	SR <sub>A</sub> <sup>3<math>\ell</math>1b</sup>	SR <sub>B</sub> <sup>3<math>\ell</math>1b</sup>	SR <sub>C</sub> <sup>3<math>\ell</math>1b</sup>	SR <sub>A</sub> <sup>1<math>\ell</math>4b</sup>	SR <sub>B</sub> <sup>1<math>\ell</math>4b</sup>	SR <sub>C</sub> <sup>1<math>\ell</math>4b</sup>
Total systematic uncertainty	20%	24%	15%	22%	17%	30%
Diboson theoretical uncertainties	6.7%	5.5%	2.2%	<1%	<1%	<1%
$t\bar{t}Z$ theoretical uncertainties	10%	10%	4.4%	<1%	<1%	<1%
$t\bar{t}$ theoretical uncertainties	—	—	—	17%	14%	22%
Other theoretical uncertainties	9.0%	6.8%	5.4%	1.6%	2.4%	1.7%
MC statistical uncertainties	8.5%	18%	6%	7.3%	5.2%	13%
Diboson fitted normalisation	4.6%	3.5%	3.8%	<1%	<1%	<1%
$t\bar{t}Z$ fitted normalisation	12%	11%	13%	<1%	<1%	<1%
$t\bar{t}$ fitted normalisation	—	—	—	3.4%	5.1%	3.3%
Fake and non-prompt leptons	—	6.5%	—	—	—	—
Pileup	4.7%	2.8%	0.6%	<1%	1.4%	<1%
Jet energy resolution	2.0%	2.7%	3.0%	5.3%	<1%	13%
Jet energy scale	1.0%	2.7%	3.5%	3.2%	5.3%	6.1%
$E_T^{\text{miss}}$ resolution	5.3%	2.6%	1.6%	6.8%	6.5%	4.0%
$b$ -tagging	2.4%	1.5%	3.0%	6.8%	2.9%	3.5%

due to the limited statistics in  $\text{CR}_{t\bar{t}Z}^{3\ell 1b}$  and theoretical uncertainties on  $t\bar{t}Z$ , while on the  $1\ell 4b$  SRs the dominant uncertainties are due to  $t\bar{t}$  modelling.

## 7 Results

The observed number of events and expected yields are shown in Table 9 for each of the six SRs. The SM backgrounds are estimated as described in Section 5. Data agree with the SM background expectation within uncertainties and thus exclusion limits for several beyond-the-SM (BSM) scenarios are extracted. Figure 4 shows the  $E_T^{\text{miss}}$  distributions after applying all the selection criteria of the SR except that on  $E_T^{\text{miss}}$ .

The HistFitter framework [87], which utilises a profile-likelihood-ratio test statistics [97], is used to estimate 95% confidence intervals using the  $\text{CL}_s$  prescription [98]. The likelihood is built as the product of a Poisson probability density function describing the observed number of events in the SR and the associated CR(s) and Gaussian distributions constraining the nuisance parameters associated with the systematic uncertainties whose widths correspond to the sizes of these uncertainties; Poisson distributions are used instead to model statistical uncertainties affecting the observed and predicted yields in the CRs. Table 9 also shows upper limits (at the 95% CL) on the visible BSM cross-section  $\sigma_{\text{vis}}$ , defined as the product of the production cross-section, acceptance and efficiency.

Model-dependent limits are also set on specific classes of SUSY models. For each signal hypothesis, the background fit is re-done taking into account the signal contamination in the CRs, which is found to be below 15% for signal models close to the Run-1 exclusion limits. All uncertainties on the SM expectation are considered, including those that are correlated between signal and background (for instance jet energy scale uncertainties), as well as all uncertainties on the signal expectation, excluding PDF and scale uncertainties on the theoretical cross-section. Since the three SRs are not orthogonal, only the SR with best expected sensitivity is used to for each signal point. “Observed limits” are calculated from the observed event yields in the SRs. “Expected limits” are calculated by setting the nominal event yield in each SR to the corresponding mean expected background.

Figure 5 shows the limits on simplified models in which pair-produced  $\tilde{t}_1$  decay with 100% branching ratio into the  $\tilde{\chi}_2^0$  and a top quark, assuming  $\text{BR}(\tilde{\chi}_2^0 \rightarrow Z\tilde{\chi}_1^0) = 0.5$  and  $\text{BR}(\tilde{\chi}_2^0 \rightarrow h\tilde{\chi}_1^0) = 0.5$ . A massless LSP and a minimum mass difference between the  $\tilde{\chi}_2^0$  and  $\tilde{\chi}_1^0$  of 130 GeV, needed to have on-shell decays for both the Higgs and  $Z$  bosons, are assumed in this model. Limits are presented in the  $\tilde{t}_1$ – $\tilde{\chi}_2^0$  mass plane. The two SRs with best expected sensitivity from the  $3\ell 1b$  and  $1\ell 4b$  selections are statistically combined to derive the limits on these models. For a  $\tilde{\chi}_2^0$  mass above 200 GeV,  $\tilde{t}_1$  mass up to about 800 GeV are excluded at 95% CL.

Limits for simplified models, in which pair-produced  $\tilde{t}_2$  decay with 100% branching ratio into the  $\tilde{t}_1$  and either a  $Z$  or a  $h$  boson, with  $\tilde{t}_1 \rightarrow t\tilde{\chi}_1^0$ , in the  $\tilde{t}_2$ – $\tilde{\chi}_1^0$  mass plane are shown in Figure 6. When considering the  $\tilde{t}_2$  decays via a  $Z$  boson, probed by the  $3\ell 1b$  selection,  $\tilde{t}_2$  masses up to 800 GeV are excluded at 95% CL for a  $\tilde{\chi}_1^0$  of about 50 GeV and  $\tilde{\chi}_1^0$  masses up to 350 GeV are excluded for  $\tilde{t}_2$  masses below 650 GeV. Assuming 100% branching ratio into  $\tilde{t}_1$  and a  $h$  boson, probed by the  $1\ell 4b$  selection,  $\tilde{t}_2$  masses up to 880 GeV at 95% CL for a  $\tilde{\chi}_1^0$  of about 50 GeV and  $\tilde{\chi}_1^0$  masses up to 260 GeV are excluded for  $\tilde{t}_2$  masses between 650 and 710 GeV.

Table 9: Background fit results for the six signal regions. The nominal expectations from MC simulation are given for comparison for those backgrounds ( $t\bar{t}Z$ , multi-boson for the  $3\ell 1b$  selection and  $t\bar{t}$  for the  $1\ell 4b$  selection) that are normalised to data in dedicated control regions. For  $SR_A^{3\ell 1b}$ ,  $SR_B^{3\ell 1b}$  and  $SR_C^{3\ell 1b}$ , the “Others” category contains the contributions from  $t\bar{t}h$ ,  $t\bar{t}WW$ ,  $t\bar{t}t$ ,  $t\bar{t}t\bar{t}$ ,  $Wh$ , and  $Zh$  production. For  $SR_A^{1\ell 4b}$ ,  $SR_B^{1\ell 4b}$  and  $SR_C^{1\ell 4b}$ , the “Others” category contains the contributions from  $t\bar{t}WW$ ,  $t\bar{t}t$ ,  $t\bar{t}t\bar{t}$ ,  $tZ$ , and  $tWZ$  production. Combined statistical and systematic uncertainties are given. Signal model-independent 95% CL upper limits on the visible BSM cross-section ( $\sigma_{\text{vis}}$ ), the visible number of signal events ( $S_{\text{obs}}^{95}$ ), the number of signal events ( $S_{\text{exp}}^{95}$ ) given the expected number of background events (and  $\pm 1\sigma$  variations on the expectation), and the discovery  $p$ -value ( $p(s = 0)$ ), all calculated with pseudo-experiments, are also shown for each signal region.

	$SR_A^{3\ell 1b}$	$SR_B^{3\ell 1b}$	$SR_C^{3\ell 1b}$
Observed events	2	1	3
Total (post-fit) SM events	$1.9 \pm 0.4$	$2.7 \pm 0.6$	$2.0 \pm 0.3$
Fit output, multi-boson	$0.26 \pm 0.08$	$0.28 \pm 0.10$	$0.23 \pm 0.05$
Fit output, $t\bar{t}Z$	$1.1 \pm 0.3$	$1.4 \pm 0.5$	$1.2 \pm 0.3$
$tZ, tWZ$	$0.43 \pm 0.23$	$0.36 \pm 0.19$	$0.19 \pm 0.10$
Fake and non-prompt leptons	$0.00^{+0.30}_{-0.00}$	$0.45 \pm 0.19$	$0.00^{+0.30}_{-0.00}$
Others	$0.09 \pm 0.02$	$0.23 \pm 0.06$	$0.36 \pm 0.06$
Fit input, multi-boson	0.35	0.37	0.30
Fit input, $t\bar{t}Z$	1.2	1.5	1.4
$S_{\text{obs}}^{95}$	4.5	3.8	5.8
$S_{\text{exp}}^{95}$	$4.2^{+1.9}_{-0.4}$	$4.9^{+1.5}_{-1.1}$	$4.4^{+1.8}_{-0.5}$
$\sigma_{\text{vis}}$ [fb]	0.13	0.10	0.16
$p(s = 0)$	0.42	0.93	0.23
	$SR_A^{1\ell 4b}$	$SR_B^{1\ell 4b}$	$SR_C^{1\ell 4b}$
Observed events	10	28	16
Total (post-fit) SM events	$13.6 \pm 3.0$	$29 \pm 5$	$10.5 \pm 3.2$
Fit output, $t\bar{t}$	$11.3 \pm 2.9$	$24 \pm 5$	$9.3 \pm 3.1$
Single top	$0.50 \pm 0.18$	$1.7 \pm 0.4$	$0.24 \pm 0.07$
$V + \text{jets}$ , multi-boson	$0.20 \pm 0.15$	$0.23 \pm 0.10$	$0.01 \pm 0.01$
$t\bar{t}h, Vh$	$0.89 \pm 0.16$	$1.19 \pm 0.35$	$0.56 \pm 0.13$
$t\bar{t}W, t\bar{t}Z$	$0.36 \pm 0.21$	$1.09 \pm 0.31$	$0.10 \pm 0.10$
Others	$0.37 \pm 0.20$	$1.33 \pm 0.69$	$0.34 \pm 0.18$
Fit input, $t\bar{t}$	7.1	14	6.0
$S_{\text{obs}}^{95}$	7.8	14.6	15.6
$S_{\text{exp}}^{95}$	$9.6^{+4.1}_{-2.3}$	$15.5^{+5.6}_{-4.4}$	$10.4^{+4.2}_{-2.6}$
$\sigma_{\text{vis}}$ [fb]	0.21	0.40	0.43
$p(s = 0)$	0.63	0.82	0.11

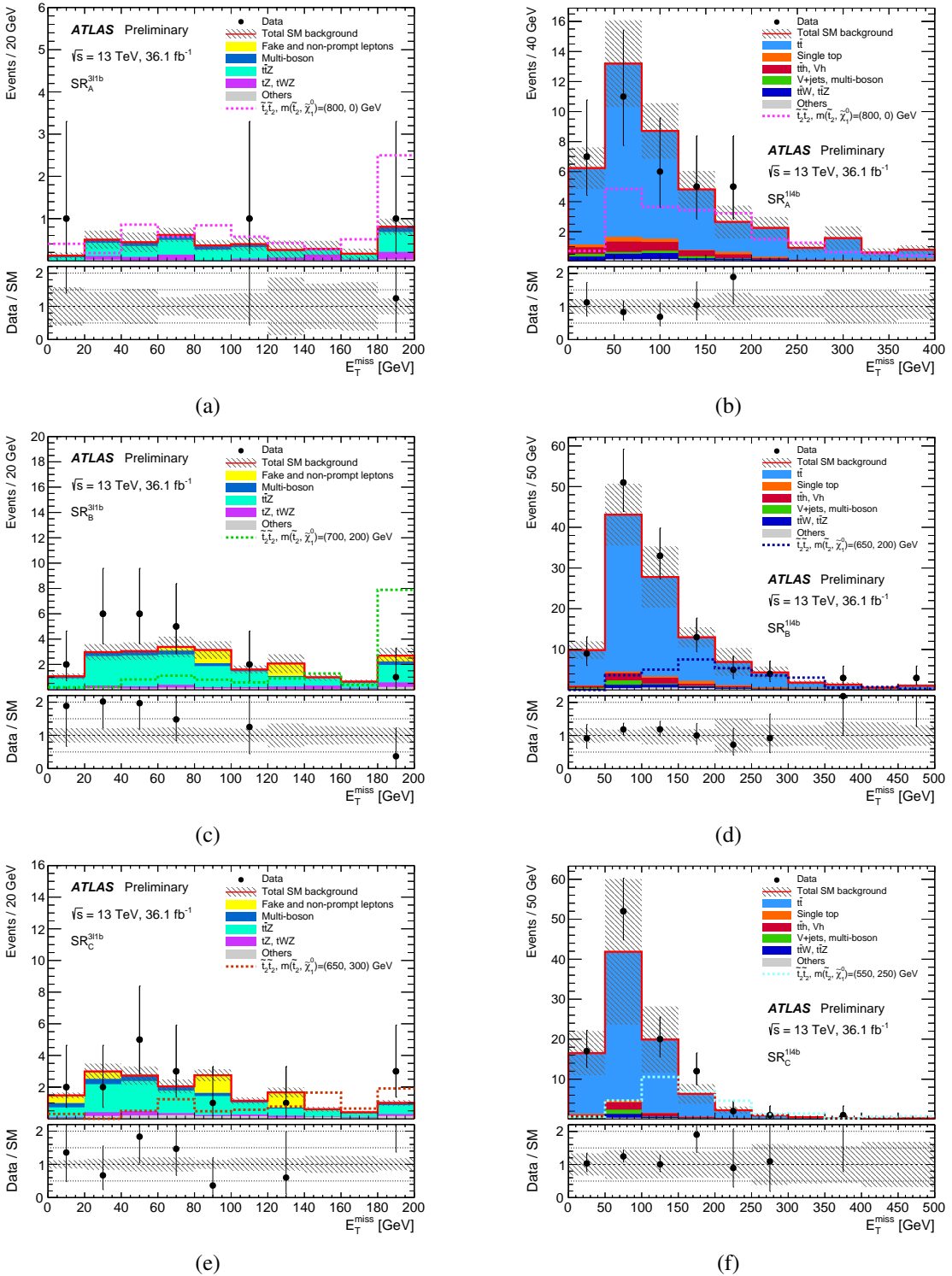


Figure 4:  $E_T^{\text{miss}}$  distribution for events passing all the signal candidate selection requirements, except that on  $E_T^{\text{miss}}$ , for (a)  $\text{SR}_A^{3\ell 1b}$ , (c)  $\text{SR}_B^{3\ell 1b}$ , (e)  $\text{SR}_C^{3\ell 1b}$  and (b)  $\text{SR}_A^{1\ell 4b}$ , (d)  $\text{SR}_B^{1\ell 4b}$ , (f)  $\text{SR}_C^{1\ell 4b}$  after the background fit described in Section 5. The contributions from all SM backgrounds are shown; the bands represent the total uncertainty. The expected distributions for signal models with  $m(\tilde{t}_2) = 700 \text{ GeV}$  and  $m(\tilde{\chi}_1^0) = 0 \text{ GeV}$ , and  $m(\tilde{t}_2) = 650 \text{ GeV}$  and  $m(\tilde{\chi}_1^0) = 250 \text{ GeV}$  are also shown as dashed lines. The last bin in all figures contains the overflow. The lower panels show the ratio of the observed data to the total SM background expectation, with the bands representing the total uncertainty on the background prediction.

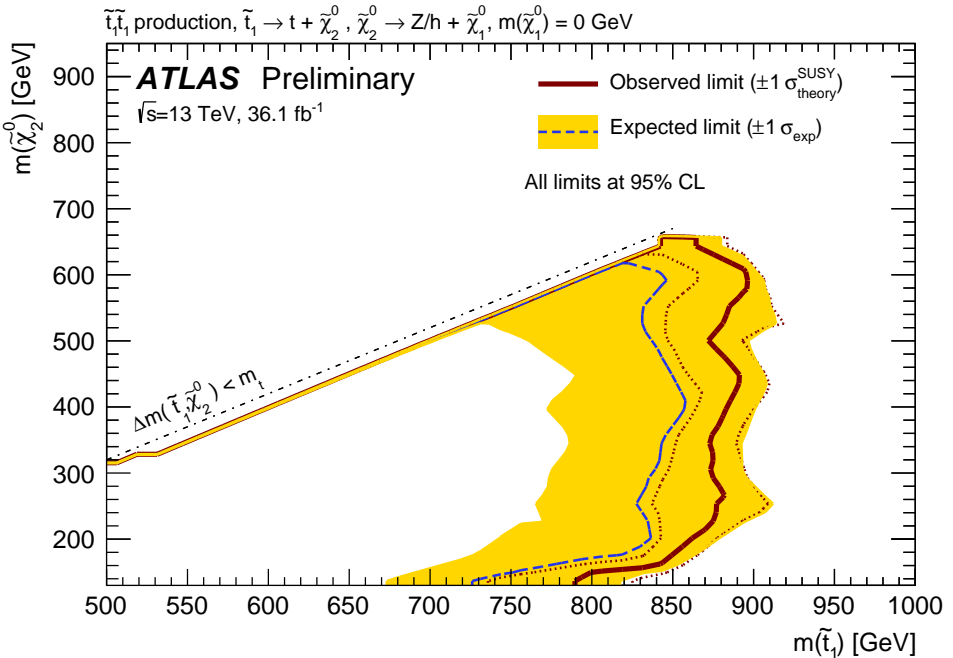
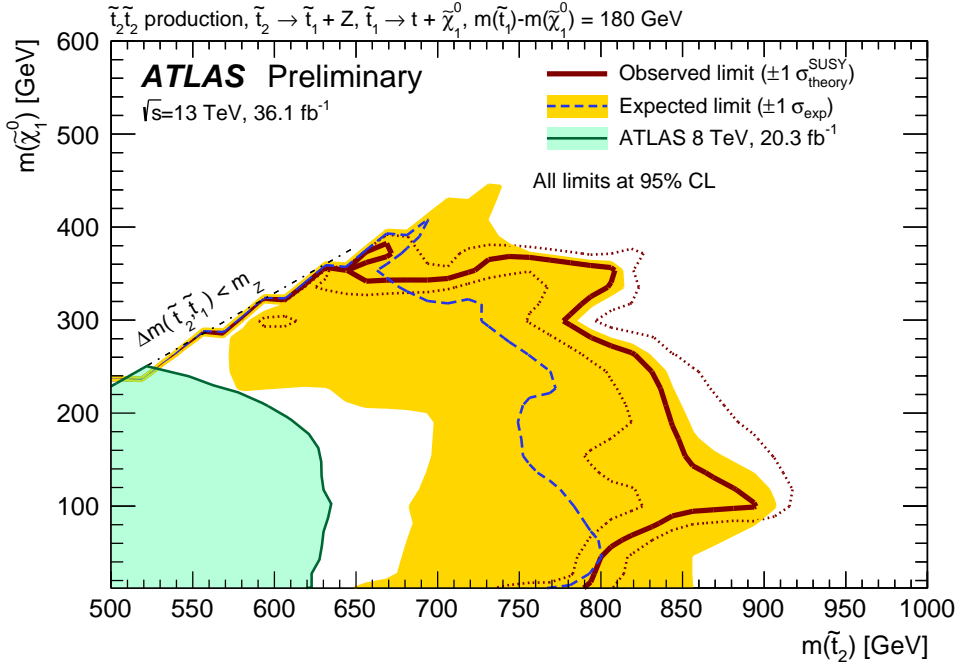
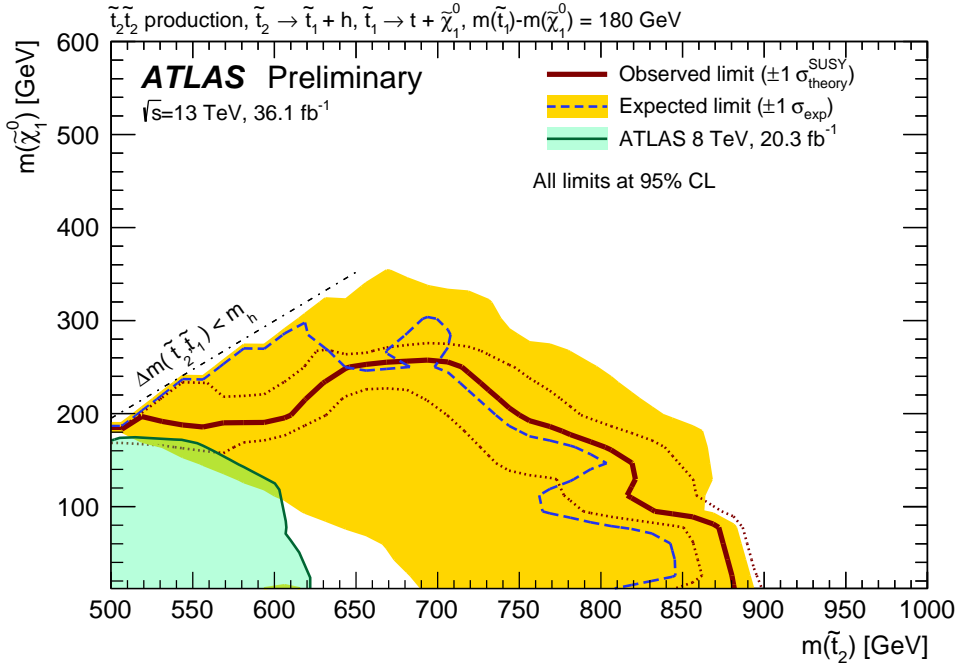


Figure 5: Exclusion limits at 95% CL from the analysis of  $36.1 \text{ fb}^{-1}$  of 13 TeV collision data on the masses of the  $\tilde{t}_1$  and  $\tilde{\chi}_2^0$ , for a fixed  $m(\tilde{\chi}_1^0) = 0 \text{ GeV}$ , assuming  $\text{BR}(\tilde{\chi}_2^0 \rightarrow Z \tilde{\chi}_1^0) = 0.5$  and  $\text{BR}(\tilde{\chi}_2^0 \rightarrow h \tilde{\chi}_1^0) = 0.5$ . The dashed line and the shaded band are the expected limit and its  $\pm 1\sigma$  uncertainty, respectively. The thick solid line is the observed limit for the central value of the signal cross-section. The expected and observed limits do not include the effect of the theoretical uncertainties on the signal cross-section. The dotted lines show the effect on the observed limit when varying the signal cross-section by  $\pm 1\sigma$  of the theoretical uncertainty.



(a)



(b)

Figure 6: Exclusion limits at 95% CL from the analysis of  $36.1 \text{ fb}^{-1}$  of 13 TeV collision data on the masses of the  $\tilde{t}_2$  and  $\tilde{\chi}_1^0$ , for a fixed  $m(\tilde{t}_2) - m(\tilde{\chi}_1^0) = 180 \text{ GeV}$  and assuming (a)  $\text{BR}(\tilde{t}_2 \rightarrow Z\tilde{t}_1) = 1$  or (b)  $\text{BR}(\tilde{t}_2 \rightarrow h\tilde{t}_1) = 1$ . The dashed line and the shaded band are the expected limit and its  $\pm 1\sigma$  uncertainty, respectively. The thick solid line is the observed limit for the central value of the signal cross-section. The expected and observed limits do not include the effect of the theoretical uncertainties on the signal cross-section. The dotted lines show the effect on the observed limit when varying the signal cross-section by  $\pm 1\sigma$  of the theoretical uncertainty. The shaded green area shows the observed exclusion from the ATLAS  $\sqrt{s} = 8 \text{ TeV}$  analysis [19, 29].

## 8 Conclusion

This note reports a search for direct top squark pair production resulting in events with either a leptonically-decaying  $Z$  boson or a pair of  $b$ -tagged jets from a Higgs boson decay, based on  $36.1 \text{ fb}^{-1}$  of proton-proton collisions at  $\sqrt{s} = 13 \text{ TeV}$  recorded by the ATLAS experiment at the LHC in 2015 and 2016. Good agreement is found between the observed events in the data and the expected SM predictions. Model-independent limits are presented, which allow reinterpretation of the results to cases of generic models that also predict similar final states in association with invisible particles. The limits exclude, at 95% confidence level, beyond-the-SM processes with visible cross-sections above  $0.11$  ( $0.21$ )  $\text{fb}$  for the  $3\ell 1b$  ( $1\ell 4b$ ) selections.

Results are also interpreted in the context of simplified models characterised by the decay chain  $\tilde{t}_1 \rightarrow t \tilde{\chi}_2^0$  with  $\tilde{\chi}_2^0 \rightarrow Z/h \tilde{\chi}_1^0$ , or  $\tilde{t}_2 \rightarrow Z/h \tilde{t}_1$  with  $\tilde{t}_1 \rightarrow t \tilde{\chi}_1^0$ . The results exclude at 95% confidence level  $\tilde{t}_2$  and  $\tilde{t}_1$  masses up to about 800 GeV, extending the region of supersymmetric parameter space covered by previous LHC searches.

## References

- [1] Yu. A. Golfand and E. P. Likhtman, *Extension of the Algebra of Poincare Group Generators and Violation of  $P$  Invariance*, JETP Lett. **13** (1971) 323, [Pisma Zh. Eksp. Teor. Fiz. **13** (1971) 452].
- [2] D. V. Volkov and V. P. Akulov, *Is the Neutrino a Goldstone Particle?*, Phys. Lett. B **46** (1973) 109.
- [3] J. Wess and B. Zumino, *Supergauge Transformations in Four-Dimensions*, Nucl. Phys. B **70** (1974) 39.
- [4] J. Wess and B. Zumino, *Supergauge Invariant Extension of Quantum Electrodynamics*, Nucl. Phys. B **78** (1974) 1.
- [5] S. Ferrara and B. Zumino, *Supergauge Invariant Yang-Mills Theories*, Nucl. Phys. B **79** (1974) 413.
- [6] A. Salam and J. A. Strathdee, *Supersymmetry and Nonabelian Gauges*, Phys. Lett. B **51** (1974) 353.
- [7] G. R. Farrar and P. Fayet, *Phenomenology of the Production, Decay, and Detection of New Hadronic States Associated with Supersymmetry*, Phys. Lett. B **76** (1978) 575.
- [8] N. Sakai, *Naturalness in Supersymmetric Guts*, Z. Phys. C **11** (1981) 153.
- [9] S. Dimopoulos, S. Raby and F. Wilczek, *Supersymmetry and the Scale of Unification*, Phys. Rev. D **24** (1981) 1681.
- [10] L. E. Ibanez and G. G. Ross, *Low-Energy Predictions in Supersymmetric Grand Unified Theories*, Phys. Lett. B **105** (1981) 439.
- [11] S. Dimopoulos and H. Georgi, *Softly Broken Supersymmetry and  $SU(5)$* , Nucl. Phys. B **193** (1981) 150.
- [12] R. Barbieri and G. F. Giudice, *Upper Bounds on Supersymmetric Particle Masses*, Nucl. Phys. B **306** (1988) 63.

- [13] B. de Carlos and J. A. Casas, *One loop analysis of the electroweak breaking in supersymmetric models and the fine tuning problem*, *Phys. Lett. B* **309** (1993) 320, arXiv: [hep-ph/9303291](#).
- [14] K. Inoue et al., *Aspects of Grand Unified Models with Softly Broken Supersymmetry*, *Prog. Theor. Phys.* **68** (1982) 927, [Erratum: *Prog. Theor. Phys.* **70** (1983) 330].
- [15] J. R. Ellis and S. Rudaz, *Search for Supersymmetry in Toponium Decays*, *Phys. Lett. B* **128** (1983) 248.
- [16] J. Alwall et al., *Searching for Directly Decaying Gluinos at the Tevatron*, *Phys. Lett. B* **666** (2008) 34, arXiv: [0803.0019 \[hep-ph\]](#).
- [17] J. Alwall, P. Schuster and N. Toro, *Simplified Models for a First Characterization of New Physics at the LHC*, *Phys. Rev. D* **79** (2009) 075020, arXiv: [0810.3921 \[hep-ph\]](#).
- [18] D. Alves et al., *Simplified Models for LHC New Physics Searches*, *J. Phys. G* **39** (2012) 105005, arXiv: [1105.2838 \[hep-ph\]](#).
- [19] ATLAS Collaboration, *ATLAS Run 1 searches for direct pair production of third-generation squarks at the Large Hadron Collider*, *Eur. Phys. J. C* **75** (2015) 510, [Erratum: *Eur. Phys. J. C* **76** (2016) 153], arXiv: [1506.08616 \[hep-ex\]](#).
- [20] ATLAS Collaboration, *The ATLAS Experiment at the CERN Large Hadron Collider*, *JINST* **3** (2008) S08003.
- [21] ATLAS Collaboration, *Search for top squarks in final states with one isolated lepton, jets, and missing transverse momentum in  $\sqrt{s} = 13$  TeV  $pp$  collisions with the ATLAS detector*, *Phys. Rev. D* **94** (2016) 052009, arXiv: [1606.03903 \[hep-ex\]](#).
- [22] ATLAS Collaboration, *Search for scalar top quark pair production in natural gauge mediated supersymmetry models with the ATLAS detector in  $pp$  collisions at  $\sqrt{s} = 7$  TeV*, *Phys. Lett. B* **715** (2012) 44, arXiv: [1204.6736 \[hep-ex\]](#).
- [23] CMS Collaboration, *Search for top-squark pair production in the single-lepton final state in  $pp$  collisions at  $\sqrt{s} = 8$  TeV*, *Eur. Phys. J. C* **73** (2013) 2677, arXiv: [1308.1586 \[hep-ex\]](#).
- [24] CMS Collaboration, *Search for supersymmetry using razor variables in events with  $b$ -tagged jets in  $pp$  collisions at  $\sqrt{s} = 8$  TeV*, *Phys. Rev. D* **91** (2015) 052018, arXiv: [1502.00300 \[hep-ex\]](#).
- [25] CMS Collaboration, *Searches for supersymmetry using the  $M_{T2}$  variable in hadronic events produced in  $pp$  collisions at 8 TeV*, *JHEP* **05** (2015) 078, arXiv: [1502.04358 \[hep-ex\]](#).
- [26] CMS Collaboration, *Search for supersymmetry in events with soft leptons, low jet multiplicity, and missing transverse energy in proton–proton collisions at  $\sqrt{s} = 8$  TeV*, *Phys. Lett. B* **759** (2016) 9, arXiv: [1512.08002 \[hep-ex\]](#).
- [27] CMS Collaboration, *Search for direct pair production of scalar top quarks in the single- and dilepton channels in proton–proton collisions at  $\sqrt{s} = 8$  TeV*, *JHEP* **07** (2016) 027, arXiv: [1602.03169 \[hep-ex\]](#).
- [28] CMS Collaboration, *Search for direct pair production of supersymmetric top quarks decaying to all-hadronic final states in  $pp$  collisions at  $\sqrt{s} = 8$  TeV*, *Eur. Phys. J. C* **76** (2016) 460, arXiv: [1603.00765 \[hep-ex\]](#).

[29] ATLAS Collaboration, *Search for direct top squark pair production in events with a Z boson, b-jets and missing transverse momentum in  $\sqrt{s} = 8$  TeV pp collisions with the ATLAS detector*, *Eur. Phys. J. C* **74** (2014) 2883, arXiv: [1403.5222 \[hep-ex\]](https://arxiv.org/abs/1403.5222).

[30] CMS Collaboration, *Search for top-squark pairs decaying into Higgs or Z bosons in pp collisions at  $\sqrt{s}=8$  TeV*, *Phys. Lett. B* **736** (2014) 371, arXiv: [1405.3886 \[hep-ex\]](https://arxiv.org/abs/1405.3886).

[31] ATLAS Collaboration, *ATLAS Insertable B-Layer Technical Design Report*, CERN-LHCC-2010-013. ATLAS-TDR-19, 2010, URL: <http://cds.cern.ch/record/1291633>.

[32] ATLAS Collaboration, *Performance of the ATLAS Trigger System in 2015*, Submitted to *Eur. Phys. J. C* (2016), arXiv: [1611.09661 \[hep-ex\]](https://arxiv.org/abs/1611.09661).

[33] ATLAS Collaboration, *Improved luminosity determination in pp collisions at  $\sqrt{s} = 7$  TeV using the ATLAS detector at the LHC*, *Eur. Phys. J. C* **73** (2013) 2518, arXiv: [1302.4393 \[hep-ex\]](https://arxiv.org/abs/1302.4393).

[34] ATLAS Collaboration, *Simulation of top-quark production for the ATLAS experiment at  $\sqrt{s} = 13$  TeV*, ATL-PHYS-PUB-2016-004, 2016, URL: <https://cds.cern.ch/record/2120417>.

[35] ATLAS Collaboration, *Monte Carlo Generators for the Production of a W or Z/ $\gamma^*$  Boson in Association with Jets at ATLAS in Run 2*, ATL-PHYS-PUB-2016-003, 2016, URL: <https://cds.cern.ch/record/2120133>.

[36] ATLAS Collaboration, *Multi-boson simulation for 13 TeV ATLAS analyses*, ATL-PHYS-PUB-2016-002, 2016, URL: <https://cds.cern.ch/record/2119986>.

[37] ATLAS Collaboration, *Modelling of the  $t\bar{t}H$  and  $t\bar{t}V$  ( $V = W, Z$ ) processes for  $\sqrt{s} = 13$  TeV ATLAS analyses*, ATL-PHYS-PUB-2016-005, 2016, URL: <https://cds.cern.ch/record/2120826>.

[38] D. J. Lange, *The EvtGen particle decay simulation package*, *Nucl. Instrum. Meth. A* **462** (2001) 152.

[39] J. Alwall et al., *The automated computation of tree-level and next-to-leading order differential cross sections, and their matching to parton shower simulations*, *JHEP* **07** (2014) 079, arXiv: [1405.0301 \[hep-ph\]](https://arxiv.org/abs/1405.0301).

[40] T. Sjöstrand, S. Mrenna and P. Z. Skands, *A Brief Introduction to PYTHIA 8.1*, *Comput. Phys. Commun.* **178** (2008) 852, arXiv: [0710.3820 \[hep-ph\]](https://arxiv.org/abs/0710.3820).

[41] W. Beenakker et al., *Squark and gluino production at hadron colliders*, *Nucl. Phys. B* **492** (1997) 51, arXiv: [hep-ph/9610490](https://arxiv.org/abs/hep-ph/9610490).

[42] A. Kulesza and L. Motyka, *Threshold resummation for squark-antisquark and gluino-pair production at the LHC*, *Phys. Rev. Lett.* **102** (2009) 111802, arXiv: [0807.2405 \[hep-ph\]](https://arxiv.org/abs/0807.2405).

[43] A. Kulesza and L. Motyka, *Soft gluon resummation for the production of gluino-gluino and squark-antisquark pairs at the LHC*, *Phys. Rev. D* **80** (2009) 095004, arXiv: [0905.4749 \[hep-ph\]](https://arxiv.org/abs/0905.4749).

[44] W. Beenakker et al., *Soft-gluon resummation for squark and gluino hadroproduction*, *JHEP* **12** (2009) 041, arXiv: [0909.4418 \[hep-ph\]](https://arxiv.org/abs/0909.4418).

[45] W. Beenakker et al., *Squark and gluino hadroproduction*, *Int. J. Mod. Phys. A* **26** (2011) 2637, arXiv: [1105.1110 \[hep-ph\]](#).

[46] H.-L. Lai et al., *New parton distributions for collider physics*, *Phys. Rev. D* **82** (2010) 074024, arXiv: [1007.2241 \[hep-ph\]](#).

[47] ATLAS Collaboration, *ATLAS Pythia8 tunes to 7 TeV data*, ATL-PHYS-PUB-2014-021, 2014, URL: <http://cds.cern.ch/record/1966419>.

[48] T. Gleisberg et al., *Event generation with SHERPA 1.1*, *JHEP* **02** (2009) 007, arXiv: [0811.4622 \[hep-ph\]](#).

[49] S. Catani et al.,  
*Vector boson production at hadron colliders: a fully exclusive QCD calculation at NNLO*, *Phys. Rev. Lett.* **103** (2009) 082001, arXiv: [0903.2120 \[hep-ph\]](#).

[50] S. Alioli et al., *A general framework for implementing NLO calculations in shower Monte Carlo programs: the POWHEG BOX*, *JHEP* **06** (2010) 043, arXiv: [1002.2581 \[hep-ph\]](#).

[51] T. Sjöstrand, S. Mrenna and P. Z. Skands, *PYTHIA 6.4 Physics and Manual*, *JHEP* **05** (2006) 026, arXiv: [hep-ph/0603175](#).

[52] M. Czakon, P. Fiedler and A. Mitov,  
*Total Top-Quark Pair-Production Cross Section at Hadron Colliders Through  $O(\alpha_S^4)$* , *Phys. Rev. Lett.* **110** (2013) 252004, arXiv: [1303.6254 \[hep-ph\]](#).

[53] M. Czakon and A. Mitov,  
*NNLO corrections to top pair production at hadron colliders: the quark-gluon reaction*, *JHEP* **01** (2013) 080, arXiv: [1210.6832 \[hep-ph\]](#).

[54] M. Czakon and A. Mitov, *NNLO corrections to top-pair production at hadron colliders: the all-fermionic scattering channels*, *JHEP* **12** (2012) 054, arXiv: [1207.0236 \[hep-ph\]](#).

[55] P. Bärnreuther, M. Czakon and A. Mitov, *Percent Level Precision Physics at the Tevatron: First Genuine NNLO QCD Corrections to  $q\bar{q} \rightarrow t\bar{t} + X$* , *Phys. Rev. Lett.* **109** (2012) 132001, arXiv: [1204.5201 \[hep-ph\]](#).

[56] M. Cacciari et al., *Top-pair production at hadron colliders with next-to-next-to-leading logarithmic soft-gluon resummation*, *Phys. Lett. B* **710** (2012) 612, arXiv: [1111.5869 \[hep-ph\]](#).

[57] M. Czakon and A. Mitov,  
*Top++: A Program for the Calculation of the Top-Pair Cross-Section at Hadron Colliders*, *Comput. Phys. Commun.* **185** (2014) 2930, arXiv: [1112.5675 \[hep-ph\]](#).

[58] P. Z. Skands, *Tuning Monte Carlo Generators: The Perugia Tunes*, *Phys. Rev. D* **82** (2010) 074018, arXiv: [1005.3457 \[hep-ph\]](#).

[59] N. Kidonakis, *Next-to-next-to-leading-order collinear and soft gluon corrections for t-channel single top quark production*, *Phys. Rev. D* **83** (2011) 091503, arXiv: [1103.2792 \[hep-ph\]](#).

[60] N. Kidonakis,  
*Two-loop soft anomalous dimensions for single top quark associated production with a W- or H-*, *Phys. Rev. D* **82** (2010) 054018, arXiv: [1005.4451 \[hep-ph\]](#).

[61] N. Kidonakis, *NNLL resummation for s-channel single top quark production*, *Phys. Rev. D* **81** (2010) 054028, arXiv: [1001.5034 \[hep-ph\]](#).

[62] G. Corcella et al., *HERWIG 6: An Event generator for hadron emission reactions with interfering gluons (including supersymmetric processes)*, *JHEP* **01** (2001) 010, arXiv: [hep-ph/0011363](#).

[63] LHC Higgs Cross Section Working Group, *Handbook of LHC Higgs Cross Sections: 2. Differential Distributions*, CERN-2012-002 (CERN, Geneva, 2012), arXiv: [1201.3084 \[hep-ph\]](#).

[64] L. Lönnblad and S. Prestel, *Matching Tree-Level Matrix Elements with Interleaved Showers*, *JHEP* **03** (2012) 019, arXiv: [1109.4829 \[hep-ph\]](#).

[65] W. Beenakker et al., *Stop production at hadron colliders*, *Nucl. Phys. B* **515** (1998) 3, arXiv: [hep-ph/9710451 \[hep-ph\]](#).

[66] W. Beenakker et al., *Supersymmetric top and bottom squark production at hadron colliders*, *JHEP* **1008** (2010) 098, arXiv: [1006.4771 \[hep-ph\]](#).

[67] C. Borschensky et al., *Squark and gluino production cross sections in pp collisions at  $\sqrt{s} = 13, 14, 33$  and  $100$  TeV*, *Eur. Phys. J. C* **74** (2014) 3174, arXiv: [1407.5066 \[hep-ph\]](#).

[68] ATLAS Collaboration, *Summary of ATLAS Pythia 8 tunes*, ATLAS-PHYS-PUB-2012-003, 2012, URL: <http://cdsweb.cern.ch/record/1474107>.

[69] A. D. Martin et al., *Parton distributions for the LHC*, *Eur. Phys. J. C* **63** (2009) 189, arXiv: [0901.0002 \[hep-ph\]](#).

[70] ATLAS Collaboration, *The ATLAS Simulation Infrastructure*, *Eur. Phys. J. C* **70** (2010) 823, arXiv: [1005.4568 \[physics.ins-det\]](#).

[71] S. Agostinelli et al., *GEANT4: A Simulation toolkit*, *Nucl. Instrum. Meth. A* **506** (2003) 250.

[72] ATLAS Collaboration, *The simulation principle and performance of the ATLAS fast calorimeter simulation FastCaloSim*, ATL-PHYS-PUB-2010-013, 2010, URL: <https://cds.cern.ch/record/1300517>.

[73] ATLAS Collaboration, *Vertex Reconstruction Performance of the ATLAS Detector at  $\sqrt{s} = 13$  TeV*, ATL-PHYS-PUB-2015-026, 2015, URL: <https://cds.cern.ch/record/2037717>.

[74] ATLAS Collaboration, *Electron efficiency measurements with the ATLAS detector using 2012 LHC proton-proton collision data*, Submitted to *Eur. Phys. J. C* (2016), arXiv: [1612.01456 \[hep-ex\]](#).

[75] ATLAS Collaboration, *Electron identification measurements in ATLAS using  $\sqrt{s} = 13$  TeV data with 50 ns bunch spacing*, ATL-PHYS-PUB-2015-041, 2015, URL: <http://cds.cern.ch/record/2048202>.

[76] ATLAS Collaboration, *Muon reconstruction performance of the ATLAS detector in proton-proton collision data at  $\sqrt{s} = 13$  TeV*, *Eur. Phys. J. C* **76** (2016) 292, arXiv: [1603.05598 \[hep-ex\]](#).

[77] ATLAS Collaboration, *Properties of jets and inputs to jet reconstruction and calibration with the ATLAS detector using proton-proton collisions at  $\sqrt{s} = 13$  TeV*, ATL-PHYS-PUB-2015-036, 2015, URL: <https://cds.cern.ch/record/2044564>.

[78] M. Cacciari, G. P. Salam and G. Soyez, *The anti- $k_t$  jet clustering algorithm*, *JHEP* **04** (2008) 063, arXiv: [0802.1189 \[hep-ph\]](#).

[79] ATLAS Collaboration, *Jet Calibration and Systematic Uncertainties for Jets Reconstructed in the ATLAS Detector at  $\sqrt{s} = 13$  TeV*, ATL-PHYS-PUB-2015-015, 2015, URL: <http://cds.cern.ch/record/2028594>.

[80] ATLAS Collaboration, *Jet global sequential corrections with the ATLAS detector in proton–proton collisions at  $\sqrt{s} = 8$  TeV*, ATLAS-CONF-2015-002, 2015, URL: <https://cds.cern.ch/record/2001682>.

[81] ATLAS Collaboration, *Performance of pile-up mitigation techniques for jets in  $pp$  collisions at  $\sqrt{s} = 8$  TeV using the ATLAS detector*, *Eur. Phys. J. C* **76** (2016) 581, arXiv: [1510.03823 \[hep-ex\]](https://arxiv.org/abs/1510.03823).

[82] ATLAS Collaboration, *Data-Quality Requirements and Event Cleaning for Jets and Missing Transverse Energy Reconstruction with the ATLAS Detector in Proton–Proton Collisions at a Center-of-Mass Energy of  $\sqrt{s} = 7$  TeV*, ATLAS-CONF-2010-038, 2010, URL: <https://cds.cern.ch/record/1277678>.

[83] ATLAS Collaboration, *Performance of  $b$ -Jet Identification in the ATLAS Experiment*, *JINST* **11** (2016) P04008, arXiv: [1512.01094 \[hep-ex\]](https://arxiv.org/abs/1512.01094).

[84] ATLAS Collaboration, *Optimisation of the ATLAS  $b$ -tagging performance for the 2016 LHC Run*, ATL-PHYS-PUB-2016-012, 2016, URL: <https://cds.cern.ch/record/2160731>.

[85] ATLAS Collaboration, *Expected performance of missing transverse momentum reconstruction for the ATLAS detector at  $\sqrt{s} = 13$  TeV*, ATL-PHYS-PUB-2015-023, 2015, URL: <http://cds.cern.ch/record/2037700>.

[86] ATLAS Collaboration, *Performance of missing transverse momentum reconstruction for the ATLAS detector in the first proton-proton collisions at  $\sqrt{s} = 13$  TeV*, ATL-PHYS-PUB-2015-027, 2015, URL: <http://cds.cern.ch/record/2037904>.

[87] M. Baak et al., *HistFitter software framework for statistical data analysis*, *Eur. Phys. J. C* **75** (2015) 153, arXiv: [1410.1280 \[hep-ex\]](https://arxiv.org/abs/1410.1280).

[88] ATLAS collaboration, *Measurement of the top quark-pair production cross section with ATLAS in  $pp$  collisions at  $\sqrt{s} = 7$  TeV*, *Eur. Phys. J. C* **71** (2011) 1577, arXiv: [1012.1792 \[hep-ex\]](https://arxiv.org/abs/1012.1792).

[89] ATLAS collaboration, *Measurement of the top quark pair production cross section in  $pp$  collisions at  $\sqrt{s} = 7$  TeV in dilepton final states with ATLAS*, *Phys. Lett. B* **707** (2012) 459, arXiv: [1108.3699 \[hep-ex\]](https://arxiv.org/abs/1108.3699).

[90] ATLAS Collaboration, *Search for the Standard Model Higgs boson decaying into  $b\bar{b}$  produced in association with top quarks decaying hadronically in  $pp$  collisions at  $\sqrt{s} = 8$  TeV with the ATLAS detector*, *JHEP* **05** (2016) 160, arXiv: [1604.03812 \[hep-ex\]](https://arxiv.org/abs/1604.03812).

[91] ATLAS Collaboration, *Jet Calibration and Systematic Uncertainties for Jets Reconstructed in the ATLAS Detector at  $\sqrt{s} = 13$  TeV*, ATL-PHYS-PUB-2015-015, 2015, URL: <https://cds.cern.ch/record/2037613>.

[92] ATLAS Collaboration, *Calibration of  $b$ -tagging using dileptonic top pair events in a combinatorial likelihood approach with the ATLAS experiment*, ATLAS-CONF-2014-004, 2014, URL: <https://cds.cern.ch/record/1664335>.

[93] ATLAS Collaboration, *Calibration of the performance of  $b$ -tagging for  $c$  and light-flavour jets in the 2012 ATLAS data*, ATLAS-CONF-2014-046, 2014, URL: <https://cds.cern.ch/record/1741020>.

[94] ATLAS Collaboration, *Muon reconstruction performance in early Run II*, ATL-PHYS-PUB-2015-037, 2015, URL: <http://cds.cern.ch/record/2047831>.

- [95] ATLAS Collaboration, *Multi-Boson Simulation for 13 TeV ATLAS Analyses*, ATL-PHYS-PUB-2016-002, 2016, URL: <http://cds.cern.ch/record/2119986>.
- [96] ATLAS Collaboration, *Modelling of the  $t\bar{t}H$  and  $t\bar{t}V$  ( $V = W, Z$ ) processes for  $\sqrt{s} = 13$  TeV ATLAS analyses*, ATL-PHYS-PUB-2015-022, 2016, URL: <http://cds.cern.ch/record/2120826>.
- [97] G. Cowan et al., *Asymptotic formulae for likelihood-based tests of new physics*, *Eur. Phys. J. C* **71** (2011) 1554, [Erratum: *Eur. Phys. J. C* **73** (2013) 2501], arXiv: [1007.1727 \[physics.data-an\]](https://arxiv.org/abs/1007.1727).
- [98] A. L. Read, *Presentation of search results: the  $CL_s$  technique*, *J. Phys. G* **28** (2002) 2693.

# Appendix

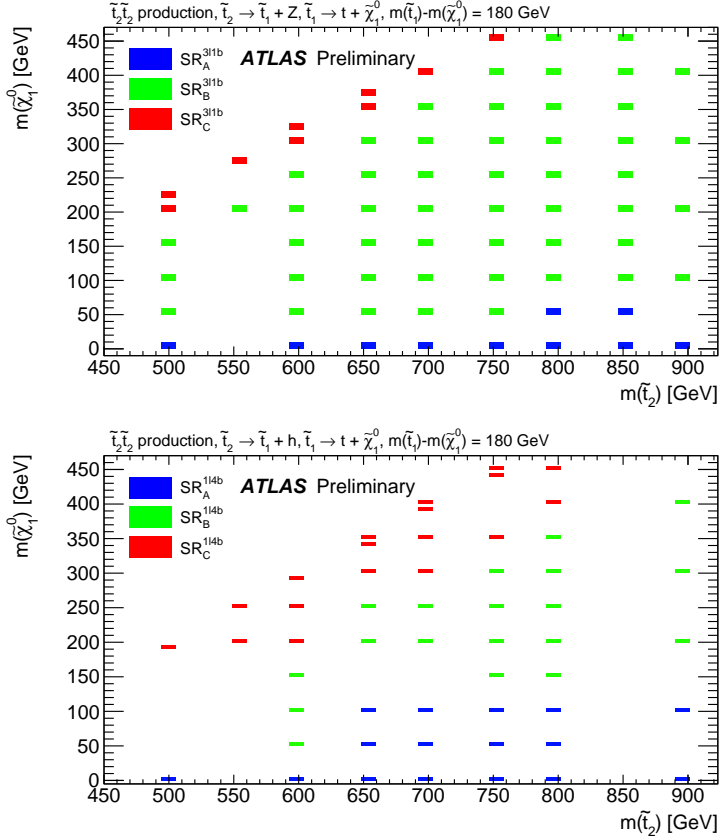


Figure 7: Illustration of the best expected signal region per signal grid point for the  $\tilde{t}_2 \rightarrow Z\tilde{t}_1$  (top) and  $\tilde{t}_2 \rightarrow h\tilde{t}_1$  (bottom) models, both with  $\tilde{t}_1 \rightarrow t\tilde{\chi}_1^0$ . This mapping is used for the final combined exclusion limits.